RSC Advances

PAPER

View Article Online
View Journal | View Issue

Cite this: *RSC Adv.*, 2020, **10**, 1261

A high-performance trace level acetone sensor using an indispensable $V_4C_3T_x$ MXene†

Wei-Na Zhao, *[a] Na Yun,[b] Zhen-Hua Dai[a] and Ye-Fei Li*[c]

The development of a stringent sensor to detect low levels of acetone, yielding the potential for the point-of-care clinical diagnosis of diabetes, is still a great challenge but is urgently required. Most studies have focused on $Ti_3C_2T_x$, yet other types of MXenes with good performance are rare. Herein, an emerging kind of MXene, $V_4C_3T_x$, has been prepared from V_4AlC_3 *via* the selective etching of the Al layer using aqueous HF at room temperature (RT), and its performance as an acetone sensor is presented. A $V_4C_3T_x$ based acetone sensor delivers good performance, as demonstrated by its low working temperature of 25 °C, low detection limit of 1 ppm (lower than the 1.8 ppm diabetes diagnosis threshold), and high selectivity towards acetone in a mixed gas of acetone and water vapor, hopefully showing promise for application in the much faster and earlier diagnosis of diabetes. $V_4C_3T_x$ MXene is used for the first time in the field of acetone detection in this work, hopefully opening up a path for the investigation of applications of MXene in gas sensors, and such exciting findings distinguish $V_4C_3T_x$ as a comparable material to the well-known $Ti_3C_2T_x$. In addition, we used DFT calculations to explore the mechanisms that result in the superior selectivity for acetone with respect to water vapor. Hopefully, the proposed mechanisms combining experimental results and theoretical study will shed light on the design and production of new high-performance acetone sensors.

Received 3rd November 2019
Accepted 18th December 2019

DOI: 10.1039/c9ra09069j

rsc.li/rsc-advances

1. Introduction

Recent years have seen an enormous amount of research highlighting oxygenated volatile organic compounds (OVOCs) owing to their threats to human health and the environment.[1–4] Among various OVOCs, acetone is one of the most promising research candidates for various industrial and medical applications, not least towards diabetes diagnosis[5–7] in human exhaled breath. Clinical analysis has shown that the acetone concentration in the exhaled breath of healthy people is 300–900 ppb, while it will increases to more than 1.8 ppm for diabetic patients.[8] Although similar work has been done relating to a highly selective trace-level acetone sensor,[9] in the face of a lower diagnosis threshold and complex physiological environment, a stringent sensor which possesses high selectivity towards acetone at the sub-ppm level still needs urgently to be addressed.

A new class of two-dimensional (2D) transition metal carbides or carbonitrides (MXenes),[10–14] with the formula $M_{n+1}XnT_x$, where M is an early transition metal (Sc, Ti, V, Cr, Zr, Nb, Mo, Ta), X is C and/or N, T is the surface termination (O, OH, and/or F) and x represents the number of termination groups, have recently received considerable interest owing to their promising applications in many diverse fields, *e.g.*, energy storage,[13,15–21] water purification,[22] electromagnetic shields,[23,24] photothermal cancer therapy,[25,26] and gas separation.[12] MXenes are fabricated by the exfoliation of ternary layered carbides and nitrides, known as MAX phases with the formula $M_{n+1}AX_n$, where $n = 1$, 2, or 3, M represents a transition metal, A represents the A-group element[27,28] in the periodic table of the elements, and X represents carbon and/or nitrogen. The exfoliation process is carried out by selectively etching the A-group element using concentrated hydrofluoric acid (HF) or hydrochloric acid (HCl) and fluoride salts or potassium hydroxide to obtain 2D carbides or carbonitrides called MXenes, which are typically functionalized with a hydroxyl (OH), oxygen (O) or fluorine (F) group.[29,30] Until now, only the following MXenes have been discovered: M_2X type,[31–34] M_3X_2 type,[30,35,36] and M_4X_3 type.[29,36] As the above list shows, it should be noted that most M_2X- and M_3X_2-types of MXenes have been obtained, but of the M_4X_3-type MXenes, only $Ta_4C_3T_x$,[10] $Nb_4C_3T_x$,[29] and $Mo_2Ti_2C_3T_x$[36] have been reported. Therefore, the development of M_4X_3-type

[a]*Guangzhou Key Laboratory of Environmental Catalysis and Pollution Control, Guangdong Key Laboratory of Environmental Catalysis and Health Risk Control, Institute of Environmental Health and Pollution Control, School of Environmental Science and Engineering, Guangdong University of Technology, Guangzhou 51006, China. E-mail: zhaowngd@gdut.edu.cn*

[b]*School of Chemical Engineering and Technology, Guangdong Industry Polytechnic, Guangzhou 510300, China*

[c]*School Collaborative Innovation Center of Chemistry for Energy Material, Key Laboratory of Computational Physical Science (Ministry of Education), Shanghai Key Laboratory of Molecular Catalysis and Innovative Materials, Department of Chemistry, Fudan University, Shanghai 200433, China. E-mail: yefeil@fudan.edu.cn*

† Electronic supplementary information (ESI) available. See DOI: 10.1039/c9ra09069j

MXenes is necessary and of great importance for expanding the application of the MXene family.

Currently, the most studied V-based MXene is V_2CT_x MXene, which has been demonstrated to be a promising electrode material for Li and Na-ion batteries according to theoretical[37,38] and experimental results.[32,39,40] Nevertheless, there are still many challenges for V_2CT_x, such as the difficulty in synthesizing the pure phase and poor stability. After studying the structure of V_2CT_x carefully, the instability of V_2CT_x can be ascribed to the fact that a three-atom-thick V_2CT_x monolayer is too thin. When the weak metallic V–Al bonds are broken in the etching process, the V–C bonds as the basic composition units of V_2CT_x are also removed, resulting in the easy decomposition of V_2CT_x. In order to overcome the problem of the thinness of V-based MXene, it is feasible to increase the thicknesses *via* the fabrication of the much thicker $V_3C_2T_x$/$V_4C_3T_x$ instead of the thinner V_2CT_x.[32,37,41] Previously, V_4AlC_3 MAX was reported in 2007,[42] boosting our confidence in the feasibility of transforming V_4AlC_3 MAX into $V_4C_3T_x$ MXene. However, we also notice that, unlike other MXenes, V_4AlC_3 cannot be produced by simple ball milling and high-temperature reaction, making it harder to synthesize $V_4C_3T_x$ MXene.

Herein, an emerging kind of MXene, $V_4C_3T_x$, is prepared by the synthesis of V_4AlC_3 with the help of Al and Co as fluxes and catalysts, while the subsequent selective etching of the Al layer from V_4AlC_3 is performed by using aqueous HF at room temperature. $V_4C_3T_x$ MXene is used in the field of acetone detection for the first time in this work. Interestingly, we found that $V_4C_3T_x$ MXene became semiconducting from the metallic V_4AlC_3 after the HF treatment. It is worth noting that $V_4C_3T_x$ MXene shows great acetone sensing performance with a low working temperature of 25 °C and a low detection limit of 1 ppm. Good acetone sensing performance makes $V_4C_3T_x$ MXene one of the few acetone sensors meeting two prerequisite conditions (high sensitivity for low concentration (sub-ppm) and high selectivity for a mixed gas), opening up a path for the investigation of applications of MXene in gas sensors.

2. Materials and methods

2.1 Chemicals

Vanadium powder (99.99%), graphite powder (99.9%), aluminum pellets (99.995%), cobalt powder (99.995%), HCl solution (30% conc.), and HF solution (48% conc.) were purchased from Sigma-Aldrich (Germany). A corundum crucible was purchased from Charslton Technologies Pte Ltd. (Singapore).

2.2 Preparation of V_4AlC_3

Originally, as with the synthesis of most MAX phases, the methods of ball milling and direct reaction of stoichiometric amounts of high-purity V, Al and C were used to obtain the V_4AlC_3 in the pure phase, but only ternary V_2AlC phase could be obtained. After many attempts, we found that Co is important for obtaining V_4AlC_3 from the reaction. At last, an optimal way was found to synthesize the V_4AlC_3 phase by using Co and Al as the catalysts and fluxes. The amounts of high-purity V, Al, Co and C in a molar ratio of 4 : 28 : 6 : 3 with a weight of 20 g were placed in a corundum crucible, and heated to 1500 °C over 10 h under flowing argon (Ar) in a tube furnace, held at 1500 °C for 30 h, then cooled to 900 °C over 30 h, and finally cooled to room temperature over 20 h. In order to obtain the V_4AlC_3 in the pure phase, the mixture was immersed in aqueous HCl to remove the excess metal of the solidified melt (the chart is shown in Fig. 1), and the possible reaction could be:

$$2Co_xAl_y + 2(2x + 3y)HCl = 2xCoCl_2 + 2yAlCl_3 + (2x + 3y)H_2\uparrow$$

The mixed solution was centrifuged at 2000 rpm for 10 min, and the supernatant was removed, then the bottom samples

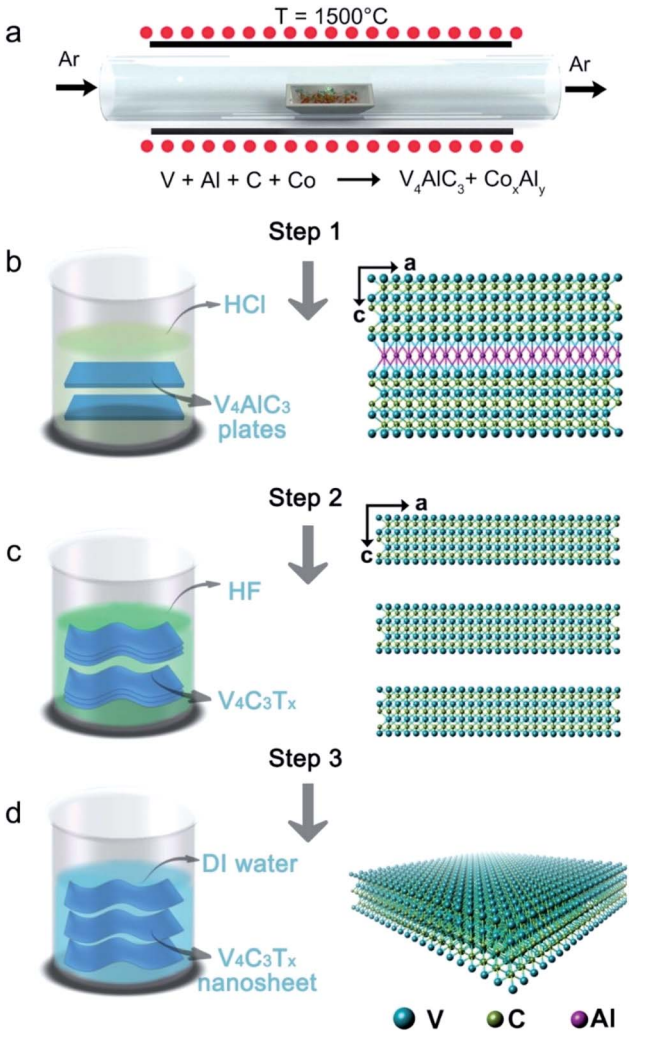

Fig. 1 The synthesis, structure, and geometrical engineering of two-dimensional $V_4C_3T_x$. (a) The setup used for the growth of a single crystal of V_4AlC_3 with the help of metal fluxes. (b) An as-synthesized V_4AlC_3 single crystal with excess metal fluxes is treated with 30% HCl solution in order to remove the metal fluxes and produce pure V_4AlC_3. (c) V_4AlC_3 powder is immersed in 48% HF solution to destroy the metallic bonds of V–Al to prepare 2D $V_4C_3T_x$ nanosheets. (d) The exfoliated $V_4C_3T_x$ nanosheets are separated *via* the sonication of $V_4C_3T_x$ powder in DI water. Step 1: HCl treatment, step 2: HF treatment, step 3: filtration, washing, sonication, and centrifugation.

were washed with deionized (DI) water. The washing step was repeated many times until the pH of the top liquid was close to the pH of DI water. Finally, after the washed samples were dried in an oven, V_4AlC_3 pure phase with metallic platelets (Fig. 2a, b and S1d†) was obtained, as confirmed by the powder XRD pattern (Fig. 2c).

2.3 Preparation of $V_4C_3T_x$ MXene

Firstly, 6 g of V_4AlC_3 single crystals was ground into a powder using a mortar, and then immersed in 110 mL of 48% concentrated HF solution at room temperature for 5 days. The resulting solution was then vacuum filtered, followed by washing with DI water until the pH reached 6. Finally, $V_4C_3T_x$ powder was obtained by filtration and freeze drying at temperature: −20 °C and vacuum: 5 Pa, for use in further characterization and experimental usage. Powder XRD patterns (Fig. 2c) and EDS spectra (Fig. 2g and Table S2†) of $V_4C_3T_x$ powder confirmed that 6 g of V_4AlC_3 had been completely transformed into 5.5 g of $V_4C_3T_x$ after HF etching for 5 days.

2.4 Fabrication of $V_4C_3T_x$ nanosheets

The $V_4C_3T_x$ powder was dispersed in DI water, and was then sonicated in an ice-bath for 5 h using an ultrasonic machine at a power of 200 W. The mixture was centrifuged for 20 min at 3000 rpm and the obtained suspension was then freeze-dried at temperature: −20 °C and vacuum: 5 Pa to obtain the final product, *i.e.* $V_4C_3T_x$ nanosheets, which were collected for further characterization and experimental usage. In addition, it should be noted that, if $V_4C_3T_x$ powder was just treated by simple sonication and centrifugation, the yield of $V_4C_3T_x$ nanosheets was less than 20%. In order to improve the rate of production, tetrabutylammonium hydroxide (TBAOH) was used to intercalate $V_4C_3T_x$ powder for delamination. Firstly, 3 g of $V_4C_3T_x$ powder was treated for 6 h with a 30% concentrated TBAOH solution. Secondly, the TBAOH treated $V_4C_3T_x$ was obtained by centrifugation for 20 min at 10 000 rpm. Thirdly, the TBAOH treated MXene was mixed with DI water and then hand-shaken for 3 minutes. Finally, the whole mixture was centrifuged for 20 min at 3000 rpm to separate the black supernatant from non-delaminated MXenes and the obtained suspension was then freeze-dried at temperature: −20 °C and vacuum: 5 Pa to obtain about 2.4 g of $V_4C_3T_x$ nanosheets. Interestingly, we found that the yield of $V_4C_3T_x$ nanosheets was improved from 25% to 80% by using the delamination agent: TBAOH.

2.5 Fabrication of $V_4C_3T_x$ quantum dots

Firstly, 2 g of V_4AlC_3 single crystals was ground into a powder using a mortar, and then immersed in 80 mL of 48% concentrated HF solution at room temperature for 10 days. The resulting solution was then filtrated and washed using DI water by turns until the pH reached 6. Secondly, the mixture was mixed with DI water and was then sonicated in an ice-bath for 2 h with a sonication power of 200 W. After centrifugation for 20 min at 10 000 rpm, the suspension was then freeze-dried at temperature: −20 °C and vacuum: 5 Pa and finally 1.0 g of $V_4C_3T_x$ nanodots was obtained, whose TEM images (Fig. 3d–f) and EDX spectra (Fig. S9†) confirmed that the V–C framework in the nanodots was retained.

2.6 Sensing measurements

For the sensing experiments and characterizations, the films obtained by vacuum filtration (Fig. S8a and S10†) were processed by freeze drying, stripping and cutting to produce the desired pieces, and two copper wires were connected by silver colloid to both ends of the $V_4C_3T_x$ film as the electrodes. A DC voltage was applied between the two electrodes, and the resistance of the $V_4C_3T_x$ film was collected as the sensing signal. The sheet resistance of the $V_4C_3T_x$ film was calculated to be ∼100 MΩ, enabling a low-power operation of the sensor to meet the requirement of ultra-low-power sensor nodes for IoT applications. The sensor device was placed in a sealed chamber, where acetone vapors at different concentrations in a nitrogen (N_2) background were fed in.

3. Results and discussion

3.1 Fabrication and characterization of $V_4C_3T_x$ nanosheets

The bulk V_4AlC_3 crystallizes in the hexagonal space group $P6_3/mmc$ with $a = b = 2.9302(4)$ Å, $c = 22.745(5)$ Å, $\alpha = \beta = 90°$, $\gamma = 120°$, and $V = 166.187$ Å^3.[42] The structure of V_4AlC_3 is characterized as a 3D V–Al–C framework consisting of seven atomic V–C–V–C–V–C–V layers connected by Al atoms with V–Al metallic bonding to form a 3D structure, as shown in Fig. S1a.† The length of the V–Al metallic bond is around 2.757 Å, longer than those of the V–C covalent bonds in the range 1.994–2.089 Å (Fig. S1b and c†). Metallic V_4AlC_3 plates of a size of several hundreds of micrometers and Co_xAl_y compounds were synthesized using a solid-state reaction (Fig. 1a, S1d and S2;† for details see the Experimental section in ESI†). After the aforementioned products were treated with HCl solution, pure V_4AlC_3 plates were obtained (Fig. 1b, step 1). In order to prepare $V_4C_3T_x$, the V_4AlC_3 plates were first ground and then treated with aqueous HF (Fig. 1c, step 2). The obtained supernatant was filtrated and washed with deionized (DI) water by turn until its pH reached 6. Finally, the $V_4C_3T_x$ nanosheets were obtained after sonication and centrifugation of the aforementioned solution (Fig. 1d, step 3).

All the synthesized V_4AlC_3 plates with a metallic luster (Fig. 2a) have a flat surface perpendicular to the *c* axis (Fig. 2b), whose pure phase was confirmed by the X-ray powder diffraction (XRD) pattern (Fig. 2c). The energy dispersive X-ray (EDX) result proved that the molar ratio of V : Al : C is 4 : 0.98 : 2.92 (Fig. 2d and e), which is consistent with the stoichiometric ratio of V_4AlC_3. In addition, the XRD pattern of single-crystal V_4AlC_3 gave strong peaks of (0002), (0004), (00010), and (00012), arising from the strong grain orientation along the *c* axis. After the treatment of V_4AlC_3 with HF, most of the diffraction peaks became much weaker or even disappeared, but the (0002) peak became quite strong (Fig. 2a), indicating that the MAX phase of V_4AlC_3 was transformed to the new MXene phase of $V_4C_3T_x$.

The shift of the (0002) peak from 7.76° to 6.04° means that the *c* lattice parameter shifts from 22.75 Å to 29.23 Å, which is

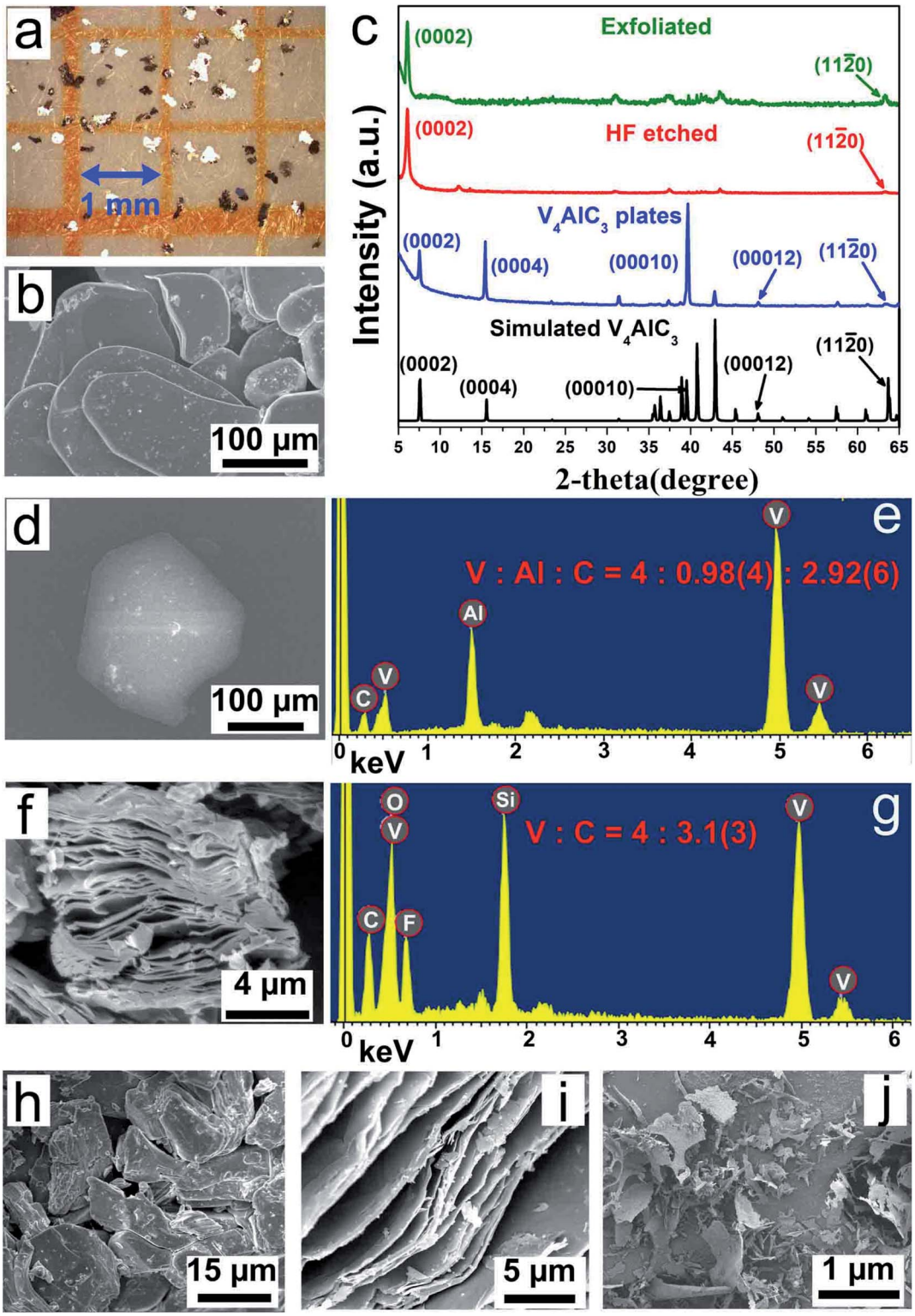

Fig. 2 The characterization and analysis of V_4AlC_3 before and after HF treatment. Optical (a) and SEM images (b) of as-synthesized V_4AlC_3 plates. (c) XRD patterns of V_4AlC_3 before and after HF (48% conc.) treatment, and exfoliated nanosheets produced *via* sonication compared to the simulated XRD pattern of V_4AlC_3. An SEM image (d) and the corresponding EDS results from a piece of V_4AlC_3 with a V : Al : C atomic ratio of 4 : 0.98 : 2.92 (e). EDS measurements taken from visibly clean surfaces of $V_4C_3T_x$ on a SiO_2/Si (280 nm oxide layer) substrate (f) prove that the V : C atomic ratio is 4 : 3.13 (g). Different-magnification SEM images of HF-treated V_4AlC_3 showing the obvious exfoliated grains (h and i). (j) An SEM image of exfoliated $V_4C_3T_x$ sheets obtained *via* sonication.

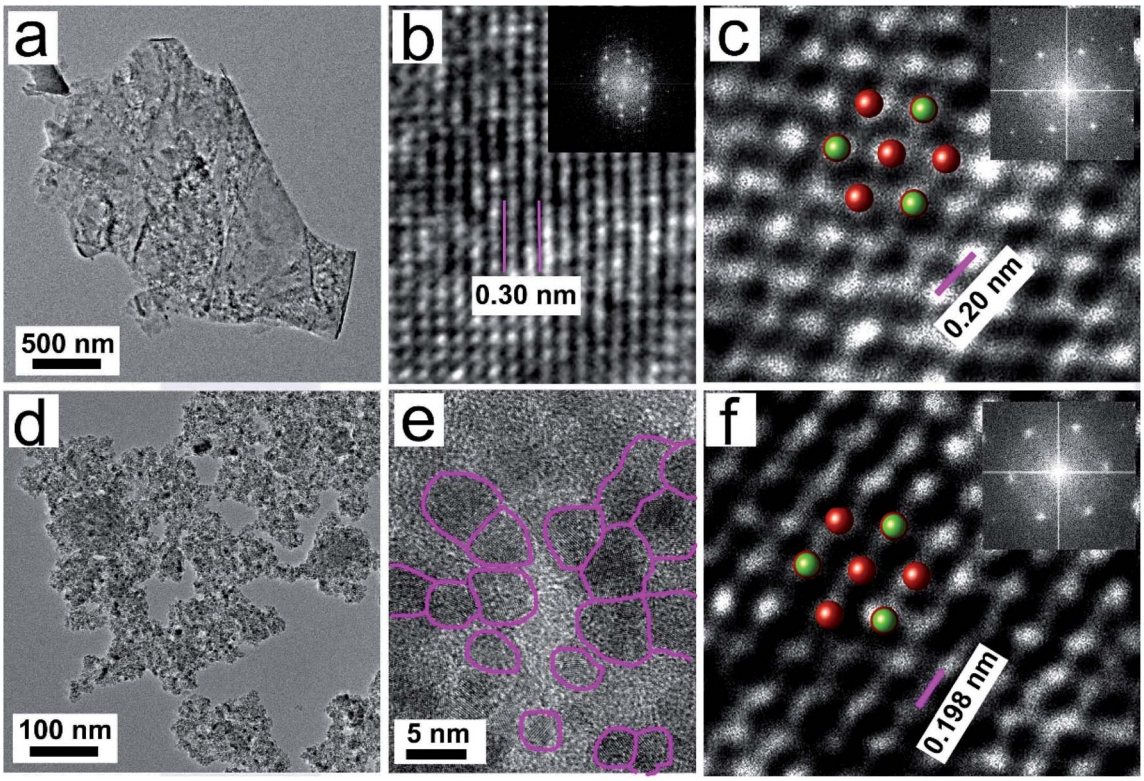

Fig. 3 TEM characterization of few-layer exfoliated $V_4C_3T_x$ nanosheets and quantum dots. Low-magnification (a) and high-resolution (b) TEM and atomic resolution *Z*-contrast STEM (c) images of $V_4C_3T_x$ nanosheets and the corresponding FFT patterns. Low-magnification (d) and high-resolution (e) TEM and atomic resolution *Z*-contrast STEM (f) images of $V_4C_3T_x$ quantum dots; the corresponding FFT pattern is shown in the inset. STEM images show the hexagonal crystal structures of $V_4C_3T_x$ nanosheets (c) and quantum dots (f). C atoms are in green and V atoms are in red.

consistent with previous reports.[29,32,37] The expansion of about 6.48 Å along the crystallographic axis *c* can be attributed to the intercalation of water between the MXene sheets during treatment. Furthermore, the domain size of ~5.6 nm along [0001] in $V_4C_3T_x$ was estimated with Scherrer's formula, revealing that the shrinkage occurs after HF treatment, which has also been reported in other MXene phases.[29,32] In addition, we also noted that, when tetrabutylammonium hydroxide (TBAOH) was used as the delamination agent to intercalate $V_4C_3T_x$ powder, the yield of $V_4C_3T_x$ nanosheets increased from 25% to 80%. The XRD patterns for $V_4C_3T_x$ before and after 6 h of TBAOH treatment (Fig. S3†) show that the (0002) peak of $V_4C_3T_x$ shifted from 6.04° to 4.2° corresponding to the *c* lattice parameter increasing from 29.23 Å to 32.72 Å, implying that, like other MXenes,[34,43] the delamination agent can also be intercalated into $V_4C_3T_x$ to improve the yield of $V_4C_3T_x$ nanoflakes.

EDX and X-ray photoelectron (XPS) spectroscopy were used to identify whether the V–C framework remained in $V_4C_3T_x$ after HF treatment. Five elements were identified in the EDX spectrum of $V_4C_3T_x$ (Fig. 2f and g): V, C and F are from the samples, while O and Si are mainly from the SiO_2 substrate. The V : C ratio is ~4 : 3.13, consistent with the expected stoichiometric ratio of 4V : 3C, indicating that the V–C framework is well preserved. This is also supported by XPS analysis where the V : C atomic ratio is ~4 : 3.24 (Fig. S4 and S5†). Notably, small amounts of F and O elements are found in the XPS spectra (Fig. S5†), which possibly come from the surface termination (*e.g.* O, OH and F) in MXene. Also, a strong signal from O is observed in the XPS, which should be from the oxygen-containing surface terminations (O or OH) or water physically absorbed between the layers, and it was also found in Nb_2CT_x, $Nb_4C_3T_x$ and V_2CT_x MXenes.[29,33,44] Based on our experimental data, and the reported reaction principles for other MXenes, such as V_2C, Nb_2C, Ti_3C_2, Ti_2C and Ta_4C_3,[10,17,32,33] the chemical reaction for the production of V_4C_3 can be written as:

$$2V_4AlC_3 + 6HF = 2V_4C_3 + 2AlF_3 + 3H_2\uparrow$$

After the main reaction, the vanadium atoms will react with the solution species in the interface between V_4C_3 and the solution, resulting in the formation of O, OH and F terminations in the surface of MXene, which was confirmed by the XPS results (Fig. S4 and S5†) and has also been observed in other MXenes.[10,32]

Scanning electron microscopy (SEM) images (Fig. 2f and h–j) show the layered structure of $V_4C_3T_x$, similar to other MXenes. The low-magnification transmission electron microscope (TEM) image shows the exfoliated $V_4C_3T_x$ nanosheets (Fig. 3a). The lattice structures of the $V_4C_3T_x$ nanosheets were examined by high-resolution TEM imaging (HRTEM, Fig. 3b and S6a†). They confirmed the single-crystalline nature of the $V_4C_3T_x$

nanosheets with a lattice spacing of ~0.30 nm (Fig. 3b). The lattice spacing agrees with the $(11\bar{2}0)$ planes of the V_4AlC_3 crystal. The atomic resolution *Z*-contrast STEM image (Fig. 3c) shows that the $V_4C_3T_x$ nanosheets maintain a hexagonal crystal structure consisting of V and C atomic columns, which is also supported by the fast Fourier transform (FFT) diffraction patterns. We also observed the formation of $V_4C_3T_x$ quantum dots after immersing V_4AlC_3 powder in aqueous HF (48% conc.) for 10 days at room temperature (Fig. 3d), which could be ascribed to the etching of the V atoms in the thinnest nanosheets or defects in V_4AlC_3 nanosheets by long-running HF treatment.

The lateral size of the $V_4C_3T_x$ quantum dots is in the range of 1–7 nm (Fig. 3e). Such quantum dots remained the hexagonal basal structure of V_4AlC_3, as confirmed by HRTEM (Fig. S6b†) and STEM (Fig. 3f) images. In addition, the specific surface area of the sample was further characterized by the Brunauer–Emmett–Teller (BET) method and N_2 adsorption/desorption isotherm analyses (Fig. S7†), showing that as-exfoliated $V_4C_3T_x$ have a high BET surface area of 156 $m^2 g^{-1}$, which can compare with those of other MXenes, such as $Ti_3C_2T_x$ of 98 $m^2 g^{-1}$,[45] $Ti_3C_2T_x$ of 4.74 $m^2 g^{-1}$,[46] $Ti_3C_2T_x/TiO_2$ nanowires of 56.45 $m^2 g^{-1}$,[46] *etc.*

3.2 Electrical transport properties of $V_4C_3T_x$ film

The electrical performance of $V_4C_3T_x$ was then evaluated. A thick film consisting of as-exfoliated $V_4C_3T_x$ nanosheets (Fig. S8a and b†) was prepared by vacuum filtration. The sheet electrical resistivity is ~3 Ω cm at room temperature measured by the four-probe method (Fig. S8c†). The sheet electrical resistivity increases exponentially at low temperature, which suggests that $V_4C_3T_x$ MXene becomes a semiconductor, presumably due to surface functionalization. The activation energy E_a for the conduction can be evaluated using the Arrhenius equation:

$$\sigma = \frac{A}{T}\exp\left(-\frac{E_a}{kT}\right)$$

where σ is the electrical conductivity, A is the conductivity constant, T is the absolute temperature, E_a is the activation energy, and k is the Boltzmann constant. The activation energy E_a for conduction, calculated from the slope of the Arrhenius plot (Fig. S8d†), is ~3.7 meV for $V_4C_3T_x$. Such a phase transition from metallic to semiconducting $V_4C_3T_x$ MXene reveals that the fully functionalized $V_4C_3T_x$ MXenes will become semiconductors with non-zero energy gaps, which was also found for its analogue MXene: V_2CT_x.[47]

Due to the large surface area and unique atomic structure of the $V_4C_3T_x$ film, it shows great potential for ultra-sensitive and highly selective gas sensing. A resistive-type $V_4C_3T_x$ film sensing device was fabricated, as shown in Fig. 4a. A DC voltage was applied between the two Cu electrodes. The resistance of the $V_4C_3T_x$ film was collected as the sensing signal. The sheet resistivity of the $V_4C_3T_x$ film was calculated to be ~1000 MΩ sq^{-1}, making it possible for ultra-low-power consuming sensor nodes for internet of things (IoT) applications. The sensor device was placed in a sealed chamber, where acetone vapors of different concentrations were fed in with nitrogen (N_2) as a carrier gas through a standing gas stream mixing method, as reported in our previous work.[48] Accordingly, this shows that acetone is sensitive to $V_4C_3T_x$ film here and can be detected accurately. More details about the experimental setup can be found in the Experimental section.

3.3 Acetone sensing properties of a $V_4C_3T_x$ based device

Good sensitivity detection of acetone down to sub-ppm has been demonstrated using $V_4C_3T_x$ film at room temperature (25 °C), as shown in Fig. 4b. It is notable that there is ~5% change in the total resistance for 1 ppm acetone, which is better than that of other reported state-of-the-art of solid-state acetone sensors at room temperature.[49–52] The selectivity of the acetone sensor toward water molecules was also characterized, as shown in Fig. 4c. At the same concentration, *i.e.* 10% v/v, the resistance change for acetone vapor is >104 higher than that for water vapor. This is much better than the recently reported high selectivity between acetone and water vapor based on protonic current measurement.[53] The inset of Fig. 4c shows the selectivity between acetone and water vapor at low concentrations from 1 ppm to 100 ppm. This shows the significant response of the sensor to acetone over a wide range, while almost no detectable signal of water vapor could be observed, suggesting the excellent selectivity towards acetone over water molecules at the low detection limit. In addition, the rise time (defined as achieving 90% of the maximum sensor response) of the acetone response (~40 s) is also much shorter than that of water vapor (~510 s). In order to evaluate the optimal operating temperature for the acetone sensor, the response of the acetone sensing at elevated temperature was characterized (Fig. 4d), showing that the response gradually increases as the temperature rises, which is similar to other nanostructured solid-state nanostructure acetone sensors. However, we also noticed that the acetone sensing response of the $V_4C_3T_x$ device at room temperature (25 °C) was large enough to meet practical applications for detecting acetone, combined with it being a rare RT acetone sensor, making the $V_4C_3T_x$ sensor a promising RT acetone sensor.

Fig. 4e shows a comparison of various unbiased acetone gas sensors based on metal oxides and nitrides, *i.e.*, In_2O_3,[54] WO_3,[55] ZnO,[56] $LaFeO_3$,[57] TiO_2,[58] GaN,[59] InN,[60] TiO_2 nanotubes,[61] TiO_2 nanoparticles,[62] 0.5% Pt–TiO_2,[63] porous α-Fe_2O_3,[64] and ZnO/graphene composites,[65] which shows that our fabricated $V_4C_3T_x$ sensor possesses the best comprehensive performance, such as good sensitivity, low concentration detected, fast response time and optimal working temperature (RT), making the $V_4C_3T_x$ sensor a promising practical acetone sensor. Therefore, $V_4C_3T_x$ film based detectors have great potential to offer a room-temperature solution for the noninvasive detection of diabetes. We hope that our results will bring more attention to MXene products for use in gas sensing detection applications.

3.4 Discussion

Our results have demonstrated that $V_4C_3T_x$ film shows high selectivity towards acetone (sub-ppm) over water vapor at room temperature, where $V_4C_3T_x$ yields superior sensing performance

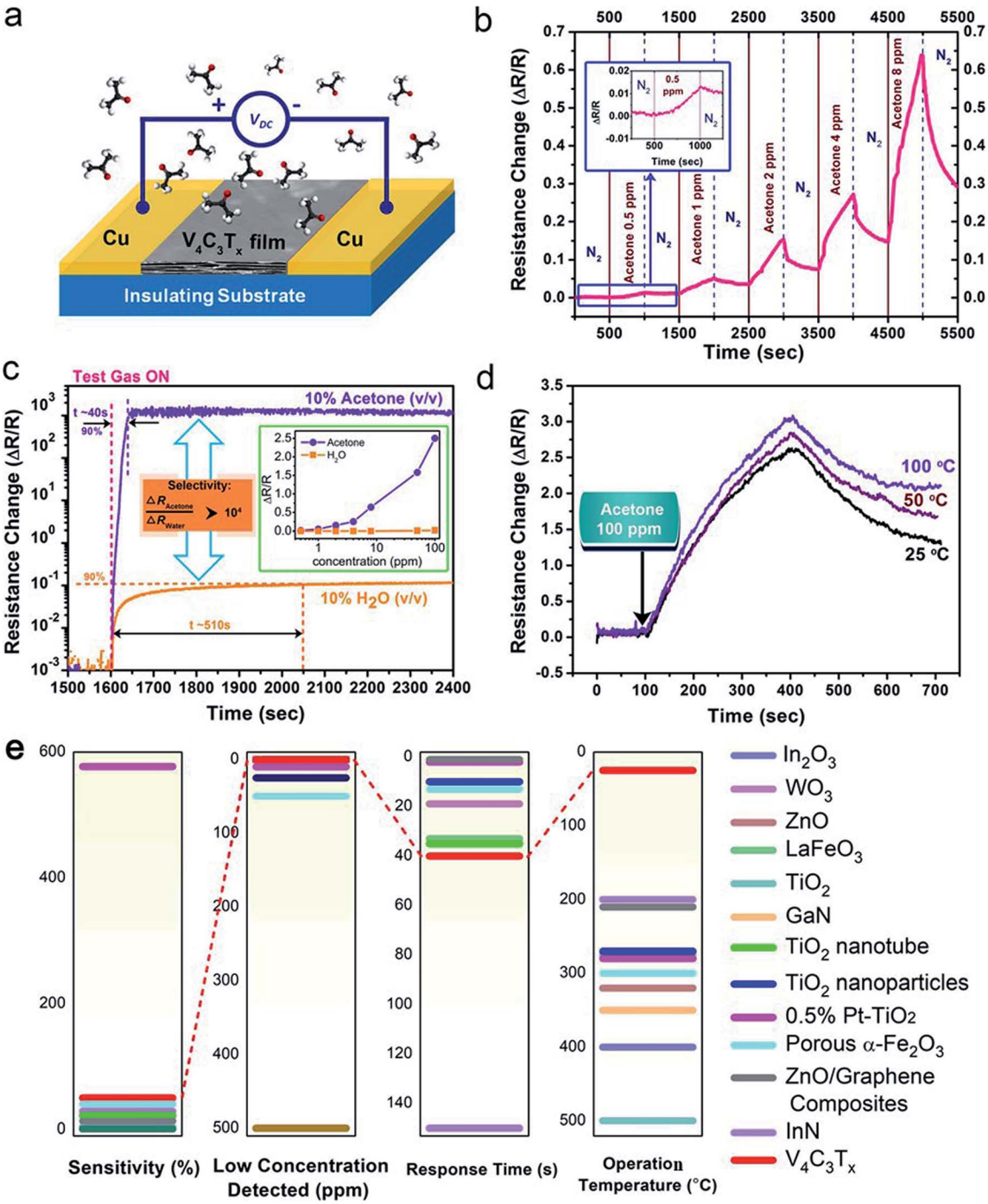

Fig. 4 The acetone sensing performance of an as-fabricated $V_4C_3T_x$ device. (a) A schematic diagram of the $V_4C_3T_x$ film sensor fabricated on an insulating substrate for mechanical support and with Cu electrodes. (b) The sensor responses of $V_4C_3T_x$ film to different concentrations of acetone from 0.5 ppm to 8 ppm at room temperature; the inset is the response to 0.5 ppm acetone. (c) A comparison of the gas sensing responses of $V_4C_3T_x$ film to 10% acetone (v/v) and 10% H_2O (v/v); the inset is the selectivity between acetone and water vapor at low concentrations, implying the excellent selectivity toward acetone over water molecules at a low detection limit. (d) The gas sensing responses of $V_4C_3T_x$ film at different temperatures of 25 °C, 50 °C, and 100 °C, respectively. (e) A comparison of various gateless acetone gas sensors with $V_4C_3T_x$ (this work) according to sensitivity, lowest concentration detected, response time, and operating temperature.

to previous work.[53] Yet it is natural to ask what causes the sensitivity of $V_4C_3T_x$ film towards acetone?

To provide insights into the mechanisms that result in superior selectivity to acetone with respect to water vapor, we first evaluated the influence of the molecule itself. It is obvious that the molecular size of acetone is much bigger than that of a water molecule. Thus the contact performance of $V_4C_3T_x$ films will be hindered ($d_1 > d_2$) due to the steric effect resulting from

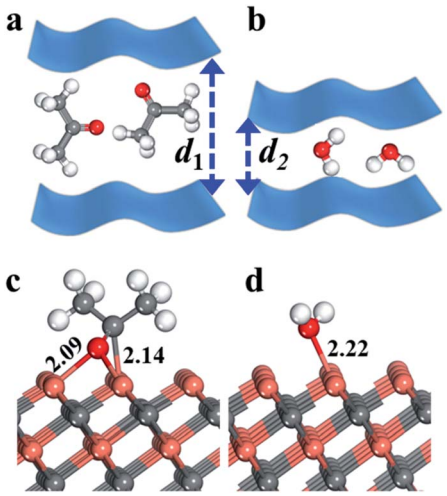

Fig. 5 A schematic diagram of the sensor responses of $V_4C_3T_x$ film to (a) acetone and (b) H_2O molecules. The DFT optimized structures of the most favourably adsorbed (c) acetone and (d) H_2O states on a V_4C_3 monolayer.

the bigger acetone molecule (a diagram is shown in Fig. 5a and b), yielding a bigger change in resistance ($\Delta R/R$) than the smaller water molecule.

In addition, we also calculated the adsorption energy of acetone and H_2O on a V_4C_3 monolayer with density functional theory (DFT) packages. In the DFT calculations, we first optimized many possible adsorption states and the most favourable optimized structures of acetone and H_2O are shown in Fig. 5c and d. As shown in Fig. 5, for acetone adsorption, acetone adsorbs on the surface three-coordinated V (V_{3c}) atoms *via* its middle C and end O atoms, forming V–C and V–O bonds, while water adsorbs on a surface V_{3c} atom, yielding an O–V_{3c} bond which is parallel with the surface V–C bond. The adsorption energy (ΔE_{ads}) per molecule (X) on the surface is defined by $\Delta E_{ads} = E[X/sur] - E[X] - E[sur]$, where E is the energy of the system based on DFT periodic calculations. Our DFT calculations show that the adsorption energies of acetone and H_2O on the V_4C_3 monolayer are −1.11 and −1.97 eV, respectively, which are consistent with the order of V–O bond lengths (2.22 Å and 2.09 Å). The large difference in adsorption behaviours (0.86 eV) corresponds to the sensitivity of $V_4C_3T_x$ film towards acetone. Similarly, an "assistive binding model" is proposed to explain the enhanced acetone sensing performance, where it is also attributed to the adsorption between target molecules and adsorbed $O^{\delta-}$ species.[9] It is hoped that the DFT calculations presented here will shed light on predictions of new high-performance acetone sensors.

4. Conclusions

In summary, assisted by catalysts and the metallic fluxes of indispensable Al and Co elements, we have synthesized a high-quality V_4AlC_3 single crystal using a solid-state reaction. An emerging MXene phase, $V_4C_3T_x$, has been obtained *via* aluminum extraction from V_4AlC_3 using aqueous HF, as confirmed by XRD, XPS and EDX. We also found that the $V_4C_3T_x$ sheets become a semiconductor after HF treatment. It is worth noting that a $V_4C_3T_x$ based acetone sensor possesses a low working temperature of 25 °C, a low detection limit of 1 ppm and high selectivity toward acetone in a mixed gas of acetone and water vapor, making it possible to diagnose diabetes. In addition, we used DFT calculations to explore the mechanisms that result in the superior selectivity toward acetone with respect to water vapor, which is due to the molecule size and adsorption behaviors. The excellent acetone sensing performance of $V_4C_3T_x$ makes it a promising material for application as a sensor for type I diabetes. The proposed mechanisms combining experimental results with theoretical study will hopefully shed light on the design and production of new high-performance acetone sensors.

Conflicts of interest

There are no conflicts to declare.

Acknowledgements

This work was supported by the National Natural Science Foundation of China (No. 21607029, 21777033), the Guangdong Natural Science Foundation (NO. 501190141), and the Science and Technology Planning Project of Guangdong Province (No. 2017B020216003). We also thank the Innovation Team Project of Guangdong Provincial Department of Education (No. 2017KCXTD012).

References

1 B. Liu, W. Zhao, Q. Jiang, Z. Ao and T. An, *Sustainable Mater. Technol.*, 2019, **21**, e00103.
2 M. Wen, G. Li, H. Liu, J. Chen, T. An and H. Yamashita, *Environ. Sci.: Nano*, 2019, **6**, 1006–1025.
3 Y. Su, Z. Ao, Y. Ji, G. Li and T. An, *Appl. Surf. Sci.*, 2018, **450**, 484–491.
4 Y. Su, W. Li, G. Li, Z. Ao and T. An, *Chin. J. Catal.*, 2019, **40**, 664–672.
5 W. Liu, X. Zhou, L. Xu, S. Zhu, S. Yang, X. Chen, B. Dong, X. Bai, G. Lu and H. Song, *Nanoscale*, 2019, **11**, 11496–11504.
6 W. Liu, L. Xu, K. Sheng, X. Zhou, B. Dong, G. Lu and H. Song, *NPG Asia Mater.*, 2018, **10**, 293–308.
7 S.-J. Choi, I. Lee, B.-H. Jang, D.-Y. Youn, W.-H. Ryu, C. O. Park and I.-D. Kim, *Anal. Chem.*, 2013, **85**, 1792–1796.
8 S. Park, *J. Alloys Compd.*, 2017, **696**, 655–662.
9 S. Dey, S. Santra, P. K. Guha and S. K. Ray, *IEEE Trans. Electron Devices*, 2019, **66**, 3568–3572.
10 M. Naguib, O. Mashtalir, J. Carle, V. Presser, J. Lu, L. Hultman, Y. Gogotsi and M. W. Barsoum, *ACS Nano*, 2012, **6**, 1322–1331.
11 Y. C. Dong, S. S. K. Mallineni, K. Maleski, H. Behlow, V. N. Mochalin, A. M. Rao, Y. Gogotsi and R. Podila, *Nano Energy*, 2018, **44**, 103–110.

12 L. Ding, Y. Y. Wei, L. B. Li, T. Zhang, H. H. Wang, J. Xue, L. X. Ding, S. Q. Wang, J. Caro and Y. Gogotsi, *Nat. Commun.*, 2018, **9**, 155.
13 B. Anasori, M. R. Lukatskaya and Y. Gogotsi, *Nat. Rev. Mater.*, 2017, **2**, 16098.
14 H. Kim, B. Anasori, Y. Gogotsi and H. N. Alshareef, *Chem. Mater.*, 2017, **29**, 6472–6479.
15 Z. F. Lin, D. Barbara, P. L. Taberna, K. L. Van Aken, B. Anasori, Y. Gogotsi and P. Simon, *J. Power Sources*, 2016, **326**, 575–579.
16 M. Q. Zhao, C. E. Ren, Z. Ling, M. R. Lukatskaya, C. F. Zhang, K. L. Van Aken, M. W. Barsoum and Y. Gogotsi, *Adv. Mater.*, 2015, **27**, 339–345.
17 M. R. Lukatskaya, O. Mashtalir, C. E. Ren, Y. Dall'Agnese, P. Rozier, P. L. Taberna, M. Naguib, P. Simon, M. W. Barsoum and Y. Gogotsi, *Science*, 2013, **341**, 1502–1505.
18 M. Ghidiu, M. R. Lukatskaya, M.-Q. Zhao, Y. Gogotsi and M. W. Barsoum, *Nature*, 2014, **516**, 78–81.
19 C. Cedric, A. Mohamed, L. V. A. Katherine, K. Narendra, G. Luisa, M. N. S. Adriana, A. Babak, N. A. Husam and G. Yury, *Adv. Electron. Mater.*, 2018, **4**, 1700339.
20 B. Anasori, M. R. Lukatskaya and Y. Gogotsi, *Nat. Rev. Mater.*, 2017, **2**, 16098.
21 Y. Xia, T. S. Mathis, M.-Q. Zhao, B. Anasori, A. Dang, Z. Zhou, H. Cho, Y. Gogotsi and S. Yang, *Nature*, 2018, **557**, 409–412.
22 L. Ding, Y. Y. Wei, Y. J. Wang, H. B. Chen, J. Caro and H. H. Wang, *Angew. Chem., Int. Ed.*, 2017, **56**, 1825–1829.
23 F. Shahzad, M. Alhabeb, C. B. Hatter, B. Anasori, S. M. Hong, C. M. Koo and Y. Gogotsi, *Science*, 2016, **353**, 1137–1140.
24 Y. Qian, H. W. Wei, J. D. Dong, Y. Z. Du, X. J. Fang, W. H. Zheng, Y. T. Sun and Z. X. Jiang, *Ceram. Int.*, 2017, **43**, 10757–10762.
25 P. Zhao, H. Jin, X. S. Lv, B. B. Huang, Y. D. Ma and Y. Dai, *Phys. Chem. Chem. Phys.*, 2018, **20**, 16551–16557.
26 H. Lin, S. S. Gao, C. Dai, Y. Chen and J. L. Shi, *J. Am. Chem. Soc.*, 2017, **139**, 16235–16247.
27 R. Kötz and M. Carlen, *Electrochim. Acta*, 2000, **45**, 2483–2498.
28 M. D. Stoller, S. Park, Y. Zhu, J. An and R. S. Ruoff, *Nano Lett.*, 2008, **8**, 3498–3502.
29 M. Ghidiu, M. Naguib, C. Shi, O. Mashtalir, L. M. Pan, B. Zhang, J. Yang, Y. Gogotsi, S. J. L. Billinge and M. W. Barsoum, *Chem. Commun.*, 2014, **50**, 9517–9520.
30 M. Naguib, V. N. Mochalin, M. W. Barsoum and Y. Gogotsi, *Adv. Mater.*, 2014, **26**, 992–1005.
31 J. Come, M. Naguib, P. Rozier, M. W. Barsoum, Y. Gogotsi, P.-L. Taberna, M. Morcrette and P. Simon, *J. Electrochem. Soc.*, 2012, **159**, A1368–A1373.
32 M. Naguib, J. Halim, J. Lu, K. M. Cook, L. Hultman, Y. Gogotsi and M. W. Barsoum, *J. Am. Chem. Soc.*, 2013, **135**, 15966–15969.
33 O. Mashtalir, M. R. Lukatskaya, M.-Q. Zhao, M. W. Barsoum and Y. Gogotsi, *Adv. Mater.*, 2015, **27**, 3501–3506.
34 O. Mashtalir, M. Naguib, V. N. Mochalin, Y. Dall'Agnese, M. Heon, M. W. Barsoum and Y. Gogotsi, *Nat. Commun.*, 2013, **4**, 1716.
35 M. Naguib and Y. Gogotsi, *Acc. Chem. Res.*, 2015, **48**, 128–135.
36 B. Anasori, Y. Xie, M. Beidaghi, J. Lu, B. C. Hosler, L. Hultman, P. R. C. Kent, Y. Gogotsi and M. W. Barsoum, *ACS Nano*, 2015, **9**, 9507–9516.
37 Y. Xie, Y. Dall'Agnese, M. Naguib, Y. Gogotsi, M. W. Barsoum, H. L. Zhuang and P. R. C. Kent, *ACS Nano*, 2014, **8**, 9606–9615.
38 J. Hu, B. Xu, C. Ouyang, S. A. Yang and Y. Yao, *J. Phys. Chem. C*, 2014, **118**, 24274–24281.
39 Y. Dall'Agnese, P.-L. Taberna, Y. Gogotsi and P. Simon, *J. Phys. Chem. Lett.*, 2015, **6**, 2305–2309.
40 J. Zhou, S. Gao, Z. Guo and Z. Sun, *Ceram. Int.*, 2017, **43**, 11450–11454.
41 L. M. Azofra, N. Li, D. R. MacFarlane and C. Sun, *Energy Environ. Sci.*, 2016, **9**, 2545–2549.
42 J. Etzkorn, M. Ade and H. Hillebrecht, *Inorg. Chem.*, 2007, **46**, 7646–7653.
43 X. Jinnan, W. Zhiqiang, C. Yuyan, L. Dujuan, C. Liang, Y. Xiaojing, L. Zhuang, M. Renzhi, S. Takayoshi and G. Fengxia, *Angew. Chem., Int. Ed.*, 2016, **128**, 14789–14794.
44 J. Feng, X. Sun, C. Wu, L. Peng, C. Lin, S. Hu, J. Yang and Y. Xie, *J. Am. Chem. Soc.*, 2011, **133**, 17832–17838.
45 Y. Dall'Agnese, M. R. Lukatskaya, K. M. Cook, P. L. Taberna, Y. Gogotsi and P. Simon, *Electrochem. Commun.*, 2014, **48**, 118–122.
46 M. J. Cao, F. Wang, L. Wang, W. L. Wu, W. J. Lv and J. F. Zhu, *J. Electrochem. Soc.*, 2017, **164**, A3933–A3942.
47 M. Khazaei, M. Arai, T. Sasaki, C.-Y. Chung, N. S. Venkataramanan, M. Estili, Y. Sakka and Y. Kawazoe, *Adv. Funct. Mater.*, 2013, **23**, 2185–2192.
48 K. Zhang, J. P. Zou and Q. Zhang, *Nanotechnology*, 2015, **26**, 455501.
49 M. Righettoni, A. Tricoli, S. Gass, A. Schmid, A. Amann and S. E. Pratsinis, *Anal. Chim. Acta*, 2012, **738**, 69–75.
50 L. L. Deng, C. X. Zhao, Y. Ma, S. S. Chen and G. Xu, *Anal. Methods*, 2013, **5**, 3709–3713.
51 Q. Fengdong, Y. Yao, G. Rohiverth and Y. Minghui, *Small*, 2016, **12**, 3128–3133.
52 S. J. Kim, H.-J. Koh, C. E. Ren, O. Kwon, K. Maleski, S.-Y. Cho, B. Anasori, C.-K. Kim, Y.-K. Choi, J. Kim, Y. Gogotsi and H.-T. Jung, *ACS Nano*, 2018, **12**, 986–993.
53 J. P. Zou, K. Zhang and Q. Zhang, *IEEE Sens. J.*, 2016, **16**, 8884–8889.
54 A. Vomiero, S. Bianchi, E. Comini, G. Faglia, M. Ferroni and G. Sberveglieri, *Cryst. Growth Des.*, 2007, **7**, 2500–2504.
55 Z.-G. Wang, M.-R. Zhang, H.-D. Peng, Q.-M. Jiang, F. Hou, Z.-L. Zhu and G.-B. Pan, *Chem. Lett.*, 2018, **47**, 518–519.
56 D. Manish and A. Anil, *Indian J. Pure Appl. Phys.*, 2018, **56**, 367–372.
57 P. A. Murade, V. S. Sangawar, G. N. Chaudhari, V. D. Kapse and A. U. Bajpeyee, *Curr. Appl. Phys.*, 2011, **11**, 451–456.
58 A. Teleki, S. E. Pratsinis, K. Kalyanasundaram and P. I. Gouma, *Sens. Actuators, B*, 2006, **119**, 683–690.
59 Y. S. Lin, K. H. Lin, Y. M. Chang and J. A. Yeh, *Surf. Sci.*, 2012, **606**, L1–L4.
60 K. W. Kao, M. C. Hsu, Y. H. Chang, S. Gwo and J. A. Yeh, *Sensors*, 2012, **12**, 7157–7168.

61 B. Bhowmik, A. Hazra, K. Dutta and P. Bhattacharyya, *IEEE Trans. Device Mater. Reliab.*, 2014, **14**, 961–967.
62 S. T. Navale, Z. B. Yang, C. Liu, P. J. Cao, V. B. Patil, N. S. Ramgir, R. S. Mane and F. J. Stadler, *Sens. Actuators, B*, 2018, **255**, 1701–1710.
63 X. Xinxin, C. Nan, Y. Yue, Z. Rongjun, W. Zhezhe, W. Zidong, Z. Tong and W. Yude, *Phys. Status Solidi A*, 2018, **215**, 1800100.
64 H. Fu, X. Wang, P. Wang, Z. Wang, H. Ren and C.-C. Wang, *Dalton Trans.*, 2018, **47**, 9014–9020.
65 H. Zhang, Y. Cen, Y. Du and S. Ruan, *Sensors*, 2016, **16**, 1876.